



1 **Effects of three-dimensional electric field on saltation**
2 **during dust storms: An observational and numerical**
3 **study**

4
5 Huan Zhang^{1,2}, You-He Zhou^{1,2}

6
7 ¹Department of Mechanics, College of Civil Engineering and Mechanics, Lanzhou
8 University, Lanzhou 730000, PR China.

9 ²Key Laboratory of Mechanics on Disaster and Environment in Western China, The
10 Ministry of Education of China, Lanzhou 730000, PR China.

11
12 Correspondence to: You-He Zhou (zhouyh@lzu.edu.cn)

13



1 **Abstract.** Particle tribo-electrification being ubiquitous in nature and industry,
2 potentially plays a key role in dust events, including the lifting and transport of sand
3 and dust particles. However, the properties of electric field (E-field) and its influences
4 on saltation during dust storms remain obscure as the high complexity of dust storms
5 and the existing numerical studies mainly limited to one-dimensional (1-D) E-field.
6 Here, we quantify the effects of real three-dimensional (3-D) E-field on saltation,
7 through a combination of field observations and numerical modelling. The 3-D E-fields
8 in the sub-meter layer from 0.05 to 0.7 m above the ground during a dust storm are
9 measured at Qingtu Lake Observation Array site. The measured results show that each
10 component of the 3-D E-field data nearly collapses on a single 3-order polynomial
11 curve when normalized. Interestingly, the vertical component of the 3-D E-field
12 increases with increasing height in the saltation layer during dust storms. Such 3-D E-
13 field data close to the ground within a few centimeters has never been reported and
14 formulated before. Using the discrete element method, we then develop a
15 comprehensive saltation model, in which the tribo-electrification between particle-
16 particle midair collisions is explicitly accounted for, allowing us to evaluate the tribo-
17 electrification in saltation properly. By combining the results of measurements and
18 modelling, we find that although the vertical component of the E-field (i.e. 1-D E-field)
19 inhibits sand transport, 3-D E-field enhances sand transport substantially. Furthermore,
20 the model predicts that 3-D E-field enhances the total mass flux by up to 63%. This
21 suggests that a truly 3-D E-field consideration is necessary if one is to explain precisely
22 how the E-field affects saltation during dust storms. These results will further improve
23 our understanding of particle tribo-electrification in saltation and help to provide more
24 accurate characterizations of sand and dust transport during dust storms.

25

26 **1. Introduction**

27 Contact- or tribo-electrification is a ubiquitous phenomenon in dust events
28 (Harrison et al., 2016; Kok and Renno, 2008; Lacks and Sankaran, 2011; Schmidt et al.,
29 1998; Zheng et al., 2003). The pioneering electric field (E-field) measurements in dust



1 storms by W. A. Douglas Rudge showed that the vertical atmospheric E-field was
2 substantially increased to 5-10 kV m⁻¹ and reversed its direction (became upward-
3 pointing) during a severe dust storm (Rudge, 1913). Later measurements in dust
4 storms found downward-pointing (Esposito et al., 2016), upward-pointing (Bo and
5 Zheng, 2013; Yair et al., 2016; Zhang and Zheng, 2018), and even alternating vertical
6 E-field which continually reverses direction (Kamra, 1972; Williams et al., 2009), with
7 the magnitude of up to ~100 kV m⁻¹.

8 The significant influences of E-field on the lifting and transport of sand and dust
9 particles have been verified, both numerically (e.g. Kok and Renno, 2008; Zhang et al.,
10 2014) and experimentally (e.g. Esposito et al., 2016; Rasmussen et al., 2009). The
11 effects of E-field on saltation, however, remain obscure. A clear discrepancy between
12 numerical simulation and field measurement is that: numerical simulation showed a
13 reduction in saltation mass flux by E-field (e.g. Kok and Renno, 2008; Zheng et al., 2003),
14 whereas recent field measurements found a dramatic increase in dust concentration
15 (up to a factor of 10) by E-field (Esposito et al., 2016), suggesting that E-field might
16 enhance saltation mass flux. This is probably because most previous numerical
17 simulations only considered the vertical component of the E-field (i.e. 1-D), but there
18 also in fact exist streamwise and spanwise components of E-field in dust events. For
19 example, Jackson and Farrell (2006) recorded the horizontal component of the E-field
20 of up to 120 kV m⁻¹ in dust devils. Zhang and Zheng (2018) also found the streamwise
21 and spanwise components (termed horizontal component) of the E-field of up to 150
22 kV m⁻¹ in dust storms. Hence, E-field is actually three-dimensional (3-D). In many cases,
23 the magnitude of the horizontal component is larger than that of the vertical
24 component. The horizontal component should therefore not be neglected when
25 evaluating the role of E-field in saltation during dust storms.

26 Most field observations, such as Schmidt et al. (1998) and Bo et al. (2014), studied
27 the electrical properties of sand particles in dust events. However, these studies are
28 generally not conclusive because the charge transfer between contacting particles are
29 sensitive to ambient conditions. For example, Schmidt et al. (1998) found that the



1 mean charge-to-mass ratio of saltating particles at 5 cm height was $+60 \mu\text{C kg}^{-1}$, which
2 did not agree with their finding of upward-pointing vertical E-field. This
3 inconclusiveness may be attributed to environmental (lurking) factors, such as relative
4 humidity, soil moisture, surface crust, etc., are not fully controllable (recorded) in the
5 field observations. The uncertainties in field observations provide motivation for
6 numerical studies of the particle tribo-electrification in saltation. In addition, unlike
7 pure saltation (that is, no suspended dust particles), the dust storm is a very complex
8 dusty phenomenon that is made up by numerous polydisperse particles embedded in
9 a high Reynolds-number turbulent flow. Such high complexity of dust storms
10 challenges the accurate simulation of 3-D E-field in dust storms. It is therefore more
11 straightforward to characterize 3-D E-field experimentally.

12 In this study, we evaluate the effects of 3-D E-field on saltation during dust storms
13 by combining measurements and modelling. To reveal the properties of 3-D E-field, we
14 simultaneously measured the 3-D E-fields in the sub-meter layer from 0.05 to 0.7 m
15 above the ground during a dust storm. Such vertical profile of 3-D E-field in the sub-
16 meter layer has not been previously characterized. To reveal how 3-D E-field affects
17 saltation, we develop a comprehensive numerical model of particle tribo-
18 electrification in saltation. In this model, the charge transfers between contacting
19 particles are explicitly calculated, but the 3-D E-field is formulated directly based on
20 the data measured in our measurements, due to its huge challenges in modelling. The
21 effects of various important parameters, such as the density of charged species, the
22 coefficient of restitution, and the E-field intensity factors, are also investigated and
23 described herein.

24

25 **2. Field campaign**

26 **2.1 Observational set-up and uncertainty**

27 We performed 3-D E-field measurements at the Qingtu Lake Observation Array
28 (QLOA) site (approximately $39^{\circ}12'27''$ N, $103^{\circ}40'03''$ E, as shown in Fig. 1a), in
29 May, 2014. The measured physical quantities include: wind velocities at four heights



1 measured by the sonic anemometers (CSAT3B, Campbell Scientific, Inc.) with 50 Hz
2 sampling frequency; number of saltating particle passing through the measurement
3 area (2 mm×25 mm) per second at 6 heights measured by sand particle counter (SPC-
4 91, Niigata Electric Co., Ltd.) with 1 Hz sampling frequency, thus providing an
5 estimation of the size distribution of saltating particles, saltation mass flux, and
6 saltation height (Text S1 in the Supplement); 3-D E-field at five heights measured by
7 the vibrating-reed E-field mill (VREFM, developed by Lanzhou University) with 1 Hz
8 sampling frequency. The layout of all instruments is shown in Fig. 1b. All instruments
9 are powered by solar panels. The detailed descriptions of the QLOA site and VREFM
10 sensor can be found in our previous studies (e.g. Zhang et al., 2017; Zheng, 2013).

11 The measurement uncertainties in our field campaign are threefold: wind velocity
12 (CSAT3B), particle mass flux (SPC-91), and E-field (VREFM). The CSAT3B is factory
13 calibrated with accuracy of $\pm 8 \text{ cm s}^{-1}$. The SPC-91 is factory calibrated by a set of
14 filamentation wires of equivalent diameters of 0.138 to 0.451 mm, with uncertainty of
15 $\pm 0.015 \text{ mm}$. The VREFM used in the field measurements is carefully calibrated and
16 selected in our lab by a parallel-plate E-field calibrator (Zhang et al., 2017), and its
17 maximum uncertainties range from $\sim 1.38 \%$ to $\sim 2.24 \%$ (see Text S2 in the Supplement).

18 19 **2.2 Data analysis**

20 In general, the actual wind direction exits a specific angle from the prevailing wind
21 direction. A projection step is therefore needed to obtain the streamwise E-field, E_1 ,
22 and spanwise E-field, E_2 . For example, E_1 is equal to the sum of the projection of the
23 measured E_x and E_y (E-field in the direction of x and y axes, as shown in Fig. 1b)
24 to the streamwise wind direction.

25 After completing the projection step, we then perform the following steps
26 sequentially to reveal the pattern of 3-D E-field in the sub-meter layer: (1) estimating
27 time-varying mean values of E-field; (2) computing height-averaged time-varying mean
28 in the measurement region from 0.05 to 0.7 m above the ground; (3) normalizing E-
29 field by height-averaged mean values; and (4) finally fitting the vertical profiles of



1 normalized E-field by the 3-order polynomial functions. It is worth noting that the
2 measured time series in dust storms are generally non-stationary when viewed as a
3 whole (e.g. Zhang and Zheng, 2018). In such cases, the statistical values are time-
4 varying. Here, we use the empirical mode decomposition (EMD) method proposed by
5 Huang et al. (1998), which is widely used in various geophysical studies (Huang and
6 Wu, 2008; Wu et al., 2011), to estimate the time-varying mean values of the measured
7 non-stationary 3-D E-field data. Each step is described in detail as follows:

8 According to the EMD method, the time series $E(t)$ can be decomposed as
9 (Huang et al., 1998)

10

$$11 \quad E(t) = \sum_{i=1}^n \xi_i + \eta_n \quad (1)$$

12

13 through a sifting process, where ξ_i ($i = 1, 2, \dots$) are the intrinsic mode functions
14 (IMFs), and η_n is a residue (which is the overall trend or mean). As an example, Fig. 2
15 shows the resulting EMD components from a measured E-field time series $E(t)$ with
16 the total of N_d data points in our field campaign, where n is specified as
17 $\log_2(N_d) - 1$. It can be seen that the time series is decomposed into a total of 13 IMFs
18 and an overall trend.

19 In this study, the time-varying mean values $\bar{E}(t)$ are defined as the sum of the
20 last four IMFs, ξ_{10} to ξ_{13} , and the residue, η_{13} , i.e.

21

$$22 \quad \bar{E}(t) = \sum_{i=10}^{13} \xi_i + \eta_{13} \quad (2)$$

23

24 which is approximately the eight-minute or longer timescale variability trend (Wu et
25 al., 2011), because the mean frequency of C10 is 2.1×10^{-3} Hz (the mean frequencies of
26 ξ_{11} - ξ_{13} are smaller than ξ_{10}), as shown in Fig. S4 in the Supplement. According to this
27 definition, the measured time series can be decomposed into a time-varying mean and



1 a stationary residue, as shown in Fig. 2a.

2 Since the 3-D E-field are measured at five heights in our field campaign, we thus
3 define the height-averaged time-varying mean values as

4

$$5 \quad \langle \overline{E}_i(t) \rangle = \frac{1}{0.7 - 0.05} \int_{0.05}^{0.7} \overline{E}_i(t, z) dz \quad (3)$$

6

7 in the range of 0.05 to 0.7 m height, in order to normalize the E-field data by a unified
8 quantity. Further, the E-field data can be normalized as

9

$$10 \quad E_i^*(t) = \frac{E_i(t)}{\langle \overline{E}_i(t) \rangle} \quad (4)$$

11

12 Additionally, to obtain the dimensionless vertical profile of 3-D E-field, the height z
13 should also be a dimensionless parameter. Here, the dimensionless height z^* is
14 defined as the ratio of height z to the saltation height z_{salt} , i.e.

15

$$16 \quad z^* = \frac{z}{z_{salt}} \quad (5)$$

17

18 where z_{salt} is defined as the height below which 99.9 % of the total mass flux is
19 present and can be estimated based on the measured SPC-91 data (see Text S1 in the
20 Supplement).

21 Finally, the dimensionless vertical profiles of 3-D E-field at different periods are
22 consistently fitted by the 3-order polynomial functions:

23

$$24 \quad E_i^* = a_{0,i} + a_{1,i}z^* + a_{2,i}z^{*2} + a_{3,i}z^{*3}, \quad i = 1,2,3 \quad (6)$$

25

26 where $i = 1, 2,$ and 3 correspond to the streamwise, spanwise, and vertical
27 components, respectively.



1 **3. Saltation model**

2 For modelling steady-state saltation, there are four primary processes, including
3 (1) particle saltating motion, (2) particle-particle midair collisions, (3) particle-bed
4 collisions, and (4) particle-wind momentum coupling (Dupont et al., 2013; Kok and
5 Renno, 2009). Also, the changes in both momentum and electrical charge of each
6 particle are taken into account in the particle-particle midair and particle-bed collisions.
7 To avoid overestimating midair collisions in 2-D simulation (Carneiro et al., 2013), we
8 simulate saltation trajectories in a real 3-D domain. We use the discrete element
9 method (DEM), which explicitly simulates each particle motion and describes the
10 collisional forces between colliding particles encompassing normal and tangential
11 components, to advance the evaluation of the effects of particle midair collisions. In
12 the following subsections, we will describe each process in detail.

14 **3.1 Size distribution of particle sample**

15 Granular materials in natural phenomena, such as sand, aerosols, pulverized
16 material, seeds of crops, etc., are made up by discrete particles with a wide range of
17 size ranging from a few micrometers to millimeters. The log-normal distribution is
18 generally used to approximate the size distribution of the sand sample (Dupont et al.,
19 2013; Marticorena and Bergametti, 1995). Thus, the mass distribution function of a
20 sand sample with two parameters, average diameter d_m , and geometric standard
21 deviation σ_p , can be written as

$$23 \quad \frac{dM(d_p)}{d\ln(d_p)} = \frac{1}{\sqrt{2\pi}\ln(\sigma_p)} \exp\left\{-\frac{[\ln(d_p) - \ln(d_m)]^2}{2[\ln(\sigma_p)]^2}\right\} \quad (7)$$

25 **3.2 Equations of saltating particles motion**

26 The total force acting on a saltating particle consists of three distinct interactions
27 (Minier, 2016). The first one refers to the wind-particle interaction, which is dominated
28 by the drag force with lifting forces such as Saffman force and Magnus force being of



1 secondary importance (Dupont et al., 2013; Kok and Renno, 2009). The second
2 interaction refers to the particle-particle collisional forces or cohesion caused by
3 physical contact between particles. Such interparticle collisional forces can be
4 described as a function of the overlaps between the colliding particles. The third
5 interaction refers to the forces due to external fields such as gravity and E-field. In this
6 study, in addition to the drag force, we also take into account the Magnus force
7 because of the remarkable rotation of saltating particles on the order of 100-1000 rev
8 s⁻¹ (Xie et al., 2007). The effects of electrostatic forces on particle motion, which are
9 significant for large wind velocity (Schmidt et al., 1998; Zheng et al., 2003), are also
10 taken into account. Consequently, the full governing equations of saltating particles
11 can be written as

12

$$13 \quad m_{p,i} \frac{d\vec{u}_{p,i}}{dt} = \vec{F}_i^d + \vec{F}_i^m + \sum_j (\vec{F}_{ij}^n + \vec{F}_{ij}^t) + m_i \vec{g} + \zeta_{p,i} \vec{E} \quad (8)$$

$$14 \quad I_i \frac{d\vec{\omega}_{p,i}}{dt} = \vec{M}_i^{w-p} + \sum_j (\vec{M}_{ij}^c + \vec{M}_{ij}^r) \quad (9)$$

15

16 where $m_{p,i}$ is the mass of the i -th particle; $\vec{u}_{p,i}$ is the velocity of the particle; \vec{F}_i^d is
17 the drag force; \vec{F}_i^m is the Magnus force; \vec{F}_{ij}^n and \vec{F}_{ij}^t are the normal and tangential
18 collisional forces from the j -th particle, respectively; \vec{g} is the gravitational
19 acceleration; $\zeta_{p,i}$ is the charge-to-mass ratio of the sand particles; \vec{E} is the 3-D E-
20 field given by our measurements; I_i is the moment of inertia; $\vec{\omega}_{p,i}$ is the angular
21 velocity of the particle; \vec{M}_i^{w-p} is the torque caused by the wind on the particle; \vec{M}_{ij}^c
22 and \vec{M}_{ij}^r are the tangential torque due to the tangential component of the particle
23 collisional forces and the rolling resistance torque, respectively. The summation Σ
24 represents considering all particles that are in contact with the i -th particle.

25

26 3.2.1 Wind-particle interactions



1 In the absence of saltating particles, the mean wind profile over a flat and
2 homogeneous surface is well approximated by the log-law (Anderson and Haff, 1988)

3

$$4 \quad u_m(z) = \frac{u_*}{\kappa} \ln \frac{z}{z_0} \quad (10)$$

5

6 where u_m is the mean streamwise wind speed; z is the height above the surface;
7 u_* is the friction velocity; $\kappa \approx 0.41$ is the von Kármán constant; z_0 is the
8 aerodynamic roughness, which varies substantially from different flow conditions and
9 can be approximately estimated as $d_m/30$ for the aeolian saltation on Earth (e.g.
10 Carneiro et al., 2013; Kok et al., 2012). In the presence of saltation, due to the
11 momentum coupling between the saltating particles and wind flow, the modified wind
12 speed gradient can be written as (e.g. Kok and Renno, 2009; Pähtz et al., 2015)

13

$$14 \quad \frac{du_m(z)}{dz} = \frac{u_*}{\kappa z} \sqrt{1 - \frac{\tau_p(z)}{\rho_a u_*^2}} \quad (11)$$

15

16 where ρ_a is the air density, $\tau_p(z)$ is the particle momentum flux and can be
17 numerically determined by (Carneiro et al., 2013; Shao, 2008)

18

$$19 \quad \tau_p(z) = - \frac{\sum m_{p,i} u_{p,i} w_{p,i}}{L_x L_y \Delta z} \quad (12)$$

20

21 with L_x , L_y , and Δz being the streamwise-, spanwise-width of the computational
22 domain, and vertical grid size, respectively; $u_{p,i}$ and $w_{p,i}$ are the streamwise and
23 vertical components of particle velocity. The summation in Eq. (12) is performed on
24 the particles located in the range of $[z, z + \Delta z]$. Once saltating particle trajectories are
25 known, the wind profile can be determined through integrating Eq. (11) with the no-
26 slip boundary condition $u_m = 0$ at $z = z_0$.

27 Since sand particles are much heavier than the air and are well smaller than the



1 Kolmogorov scales, the drag force is the dominant force affecting particle motion,
2 which is expressed by (Anderson and Haff, 1991)

3

$$4 \quad \vec{F}_i^d = -\frac{\pi d_p^2}{8} \rho_a C_d \vec{u}_r |\vec{u}_r| \quad (13)$$

5

6 where d_p is the diameter of particle; C_d is the drag coefficient; and $\vec{u}_r = \vec{u}_p - \vec{u}_w$
7 is the particle-to-wind relative velocity. The drag coefficient C_d is a function of the
8 particle Reynolds number, $Re_p = \rho_a |\vec{u}_r| d_p / \mu$, where μ is the dynamic viscosity
9 of the air. We calculate the drag coefficient by an empirical relation $C_d =$
10 $\left[(32/Re_p)^{2/3} + 1 \right]^{3/2}$, which is applicable to the regimes from Stokes flow $Re_p \ll 1$
11 to high Reynolds number turbulent flow (Cheng, 1997).

12 Additionally, we also account for the effects of particle rotation on particle motion
13 using the Magnus force expressed as (Anderson and Hallet, 1986; Loth, 2008; White
14 and Schulz, 1977)

15

$$16 \quad \vec{F}_i^m = \frac{\pi d_p^2}{8} \rho_a C_m (\vec{\omega}_{p,i} \times \vec{u}_r) \quad (14)$$

17

18 where C_m is a normalized spin lift coefficient depended on the particle Reynolds
19 number and the circumferential speed of the particle. The torque acting on a particle
20 caused by wind flow is calculated from (Anderson and Hallet, 1986; Kok and Renno,
21 2009; Shao, 2008)

22

$$23 \quad \vec{M}_i^{w-p} = \pi \mu d_i^3 \left(\frac{1}{2} \frac{du_m}{dz} - \vec{\omega}_i \right) \quad (15)$$

24

25 3.2.2 Particle-particle midair collisions

26 Under moderate conditions, saltation is a dilute flow in which the particle-particle
27 collisions are negligible. However, as wind velocity increases, midair collisions become
28 increasingly pronounced, especially in the near surface region. For spherical particles,



1 one of the most commonly-used collisional force model is the nonlinear viscoelastic
 2 model, consisting of two components, i.e. elastic and viscous forces (Brilliantov et al.,
 3 1996; Haff and Anderson, 1993; Silbert et al., 2001; Tuley et al., 2010).

4 Considering two spherical particles i and j with diameters d_i and d_j , and
 5 position vectors \vec{x}_i and \vec{x}_j , are in contact with each other. The relative velocity \vec{v}_{ij}
 6 at the contact point and its normal and tangential components, \vec{v}_{ij}^n and \vec{v}_{ij}^t , are
 7 respectively defined as (Norouzi et al., 2016; Silbert et al., 2001)

8

$$9 \quad \vec{v}_{ij} = \vec{u}_{p,i} - \vec{u}_{p,j} + 0.5(d_i \vec{\omega}_{p,i} + d_j \vec{\omega}_{p,j}) \times \vec{n}_{ij} \quad (16)$$

$$10 \quad \vec{v}_{ij}^n = (\vec{v}_{ij} \cdot \vec{n}_{ij}) \vec{n}_{ij} \quad (17)$$

$$11 \quad \vec{v}_{ij}^t = \vec{v}_{ij} - \vec{v}_{ij}^n \quad (18)$$

12

13 where $\vec{n}_{ij} = (\vec{x}_j - \vec{x}_i) / |\vec{x}_j - \vec{x}_i|$ is the unit vector in the direction from the center
 14 of particle i point toward the center of particle j . Suppose that colliding particles
 15 having identical mechanical properties with Young's modulus Y , shear modulus G ,
 16 and Poisson's ratio ν , and thus the normal collisional force can be calculated by
 17 (Brilliantov et al., 1996; Silbert et al., 2001)

18

$$19 \quad \vec{F}_{ij}^n = -\frac{4}{3} Y^* \sqrt{R^*} \delta_n^{3/2} \vec{n}_{ij} - 2 \sqrt{\frac{5}{6}} m^* S_n \beta v_n \vec{n}_{ij} \quad (19)$$

20

21 where $Y^* = Y/2/(1 - \nu^2)$ is the equivalent Young's modulus; $\delta_n = 0.5(d_i + d_j) -$
 22 $|\vec{x}_i - \vec{x}_j|$ is the normal overlap; $m^* = m_i m_j / (m_i + m_j)$ is the equivalent particle
 23 mass; $S_n = 2Y^* \sqrt{R^* \delta_n}$ is the normal contact stiffness; $R^* = d_i d_j / 2 / (d_i + d_j)$ is
 24 the equivalent particle radius; β is related to the coefficient of restitution e_n by the
 25 relationship $\beta = \ln e_n / \sqrt{(\ln e_n)^2 + \pi^2}$; and $v_n = \vec{v}_{ij} \cdot \vec{n}_{ij}$. The first term on the right-



1 hand side of Eq. (19) represents the elastic force described by Hertz's theory, and the
 2 second term represents the viscous force reflecting the inelastic collisions between
 3 sand particles. Similarly, the tangential collisional force, which is limited by the
 4 Coulomb friction, is given as (Brilliantov et al., 1996; Silbert et al., 2001)

$$5 \quad \vec{F}_{ij}^t = \begin{cases} -8G^* \sqrt{R^* \delta_n} \delta_t \vec{t}_{ij} - 2 \sqrt{\frac{5}{6}} m^* S_t \beta v_t \vec{t}_{ij}, & \text{if } |\vec{F}_{ij}^t| \leq \gamma_s |\vec{F}_{ij}^n| \\ -\gamma_s |\vec{F}_{ij}^n| \vec{t}_{ij}, & \text{if } |\vec{F}_{ij}^t| > \gamma_s |\vec{F}_{ij}^n| \end{cases} \quad (20)$$

7
 8 where $G^* = G/2/(2 - \nu)$ is the equivalent shear modulus; δ_t is the tangential
 9 overlap; $\vec{t}_{ij} = \vec{v}_{ij}^t / |\vec{v}_{ij}^t|$ is the tangential unit vector at the contact point; $S_t =$
 10 $8G^* \sqrt{R^* \delta_n}$ is the tangential stiffness; $v_t = \vec{v}_{ij} \cdot \vec{t}_{ij}$; and γ_s is the coefficient of static
 11 friction. The torque on the i -th particle arising from the j -th particle collisional force
 12 is defined as (Haff and Anderson, 1993)

$$13 \quad \vec{M}_{ij}^c = 0.5 d_i \vec{n}_{ij} \times \vec{F}_{ij}^t \quad (21)$$

15
 16 To account for the significant rolling friction, we apply a rolling resistance torque
 17 (Ai et al., 2011)

$$18 \quad \vec{M}_{ij}^r = -\gamma_r R^* |\vec{F}_{ij}^n| \vec{\omega}_{ij} \quad (22)$$

19
 20 on each colliding particle, where μ_r is the coefficient of rolling friction, and $\vec{\omega}_{ij} =$
 21 $(\vec{\omega}_{p,i} - \vec{\omega}_{p,j}) / |\vec{\omega}_{p,i} - \vec{\omega}_{p,j}|$ is the unit vector of relative angular velocity.

22 3.3 Particle-bed collisions

23
 24 As a saltating particle collides with the sand bed, it has not only a chance to
 25



1 rebound but also may eject several particles from the sand bed. For simplicity, we use
2 a probabilistic representation, termed as “splash function”, to describe the particle-
3 bed interactions quantitatively (Kok et al., 2012; Shao, 2008). Currently, the splash
4 function is primarily characterized by wind-tunnel and numerical simulations (e.g.
5 Anderson and Haff, 1991; Haff and Anderson, 1993; Rice et al., 1996). The rebounding
6 probability of a saltating particle colliding with the sand bed is approximately by
7 (Anderson and Haff, 1991)

8

$$9 \quad P_{reb} = 0.95[1 - \exp(-v_{imp})] \quad (23)$$

10

11 where v_{imp} is the impact speed of the saltating particle. The kinetic energy of the
12 rebounding particles is taken as 0.45 ± 0.22 of the impact particle (Kok and Renno,
13 2009). The rebounding angles θ and φ , as depicted in Fig. 3a, obey an exponential
14 distribution with a mean value of 40° , i.e. $\theta \sim \text{Exp}(40^\circ)$, and a normal distribution
15 with parameters $0 \pm 10^\circ$, i.e. $\varphi \sim N(0^\circ, 10^\circ)$, respectively (Dupont et al., 2013; Kok
16 and Renno, 2009).

17 It is reasonable to assume that the number of ejected particles depends on the
18 impact speed and its cross-sectional area. Thus, the number of ejected particles from
19 the k -th particle bin is (Kok and Renno, 2009)

20

$$21 \quad N_k = \frac{0.02}{\sqrt{gD_{250}}} \frac{D_{imp}}{D_{eje}^k} p_k v_{imp} \quad (24)$$

22

23 where $D_{250} = 0.25 \times 10^{-4}$ m is a reference diameter; D_{imp} and D_{eje}^k are the
24 diameter of the impact and ejected particles, respectively; and p_k is the mass
25 fraction of the k -th particle bin. The speed of the ejected particles obeys an
26 exponential distribution with mean value taken as $0.6[1 - \exp(-v_{imp}/40/\sqrt{gD_{250}})]$
27 (Kok and Renno, 2009). Similar to rebound process, the ejected angles θ and φ are



1 assumed to be $\theta \sim \text{Exp}(50^\circ)$ and $\varphi \sim \text{N}(0^\circ, 10^\circ)$.

2

3 **3.4 Particle charge exchanges**

4 In this study, the calculation of the charge transfer between sand particle
5 collisions is based on the asymmetric contact model, assuming that the electrons
6 trapped in high energy states on one particle surface can relax to the other particle
7 surface (Hu et al., 2012; Kok and Lacks, 2009). Thus, the net increment of the charge
8 of particle i after colliding with particle j , Δq_{ij} , can be determined by

9

$$10 \quad \Delta q_{ij} = -e(\rho_h^j S_j - \rho_h^i S_i) \quad (25)$$

11

12 where $e = 1.602 \times 10^{-19}$ C is the elementary charge; ρ_h^i is the density of the
13 electrons trapped in the high energy states on the surface of particle i (assuming that
14 all particles have an identical initial value ρ_h^0), which is modified as $\rho_{h,i}^{\text{after}} =$
15 $\rho_{h,i}^{\text{before}} + (\rho_h^j S_j - \rho_h^i S_i)/(\pi d_i^2)$ due to collisions between particle i and j ; S_i is the
16 particle contact area, which can be approximately calculated as a line integral along
17 the contact path L_i of particle i

18

$$19 \quad S_i = 2 \int_{L_i} \sqrt{R^* \delta_n} dl_i \quad (26)$$

20

21 where dl_i is the differential of the contact length. In general, when two particles are
22 in contact with each other, the relative sliding motion between the two particles
23 results in two unequal contact areas S_i and S_j , thus producing net charge transfer
24 Δq_{ij} between the two particles.

25

26 **3.5 Model implementation**

27 We consider polydispersed soft-spherical sand particles having log-normal mass



1 distribution in a 3-D computational domain 0.5 m×0.1 m×1.0 m (as shown in Fig. 3a),
2 with periodic boundary condition in the x and y directions. Here, the upper
3 boundary is set to be high enough so that the particle escapes from the upper
4 boundary can be avoided.

5 As shown in Fig. 3b, the model is initiated by randomly releasing 100 uncharged
6 particles, within the region below 0.3 m, and then such released particles begin to
7 move under the action of the initial log-law wind flow, triggering saltation through a
8 series of particle-bed collisions. We use cell-based collision searching algorithms,
9 which performs collision search for particles located in the target cell and its
10 neighboring cells, to find the midair colliding pairs. The random processes, particle-
11 bed collisions described previously, are simulated using a general method called the
12 inverse transformation. The particle motion and wind flow equations are integrated by
13 predictor-corrector method AB3AM4; that is, 3-order Adams-Bashforth method to
14 perform prediction and 4-order Adams-Moulton method to perform correction. One
15 of the main advantages of using such multi-step integration method is that the
16 accuracy of results is not sensitive to the detection of exact moments of collision (Tuley
17 et al., 2010). The charge transfer between the colliding pairs are caused by their
18 asymmetric contact and can be determined by Eqs. (25) and (26). When calculating
19 particle-bed charge transfer, the bed is regarded as an infinite plane. According to the
20 law of charge conservation, the surface charge density of the infinite bed plane and
21 the newly ejected particles, σ , is (Kok and Renno, 2008; Zhang et al., 2014)

22

$$23 \quad \sigma = - \int_{z_0}^{+\infty} \rho_c(z) dz \quad (27)$$

24

25 where ρ_c is the space charge density. For modelling pure saltation, the E-field is
26 calculated by the Gauss's law (e.g. Zhang et al., 2014). For modelling saltation during
27 dust storms, the 3-D E-field is directly formulated by Eq. (6) based on our field
28 measurements, as mentioned above. The variables used in this study are listed and



1 described in Table 1.

2

3 **4. Results**

4 **4.1. Vertical profiles of 3-D E-field**

5 On May 6, 2014, field measurements began at ~12:00 due to the limited power
6 supply by solar panels. As shown in Figs. 4a-4e, although the early stage of dust storm
7 has not been observed, we successfully recorded data of about 8 hours, which is
8 substantial enough to reveal the pattern of 3-D E-field. From Figs. 4a-4e, it can be seen
9 that, in general, the streamwise component (up to ~80 kV m⁻¹) and spanwise
10 component (up to ~60 kV m⁻¹) are one order of magnitude larger than the vertical
11 component of the E-field (~7 kV m⁻¹). The vertical profiles of the normalized
12 streamwise, spanwise, and vertical components of E-field are shown in Figs. 5a-5c,
13 respectively. To the best of our knowledge, these data are the first measured 3-D E-
14 field data in the sub-meter layer during dust storms. Numerous studies showed that
15 the vertical component of E-field in pure saltation decreased with increasing height
16 (e.g., Kok and Renno, 2008; Schmidt et al., 1998; Zhang et al., 2014). Interestingly, Fig.
17 5c shows that during dust storms, normalized vertical component E_3^* increases
18 monotonically as height increases in the saltation layer (i.e. $z^* \leq 1$), as distinct from
19 the vertical component in pure saltation.

20 As shown in Figs. 5a-5c, in different periods, each component of the normalized
21 3-D E-field nearly collapses on a single 3-order polynomial curve (with $R^2=0.52-0.61$,
22 see Table 2 for the details). This suggests that during dust storms, the 3-D E-field in the
23 sub-meter layer can be characterized as $\lambda_i E_i^*$ ($i = 1,2,3$), where E_i^* is described by
24 Eq. (6), and λ_i (having the units of kV m⁻¹) are termed herein as E-field intensity
25 factors which embody the saltation conditions. For example, the more dust mass
26 loading, the larger λ_i (i.e. larger E-field intensity). The fitting results of Eq. (6) are
27 listed in Table 2, with coefficients as rounded to two decimals. The formulations of the
28 3-D E-field can be readily substituted into the numerical model (i.e. Eq. 8).

29



1 **4.2. Effects of particle-particle midair collisions on saltation**

2 Before quantifying the effects of 3-D E-field on saltation by our numerical model,
3 we draw a comparison of several key physical quantities between the simulated results
4 and measurements in the case of pure saltation, in order to ensure the convergence
5 and validity of our numerical code, as shown in Figs. 6a-6c. It is clearly shown that
6 saltation eventually reaches a dynamic steady-state after ~ 4 seconds. The number of
7 the impacting particles (~ 72 grains) is equal to the sum of the rebounding (~ 50 grains)
8 and the ejected particles (~ 22 grains). At steady-state, each impacting particle, on
9 average, produces a single saltating particle, either by rebound or by ejection. As
10 shown in Fig. 6b, the total mass flux is well predicted by our numerical model, and
11 midair collisions enhance the total mass flux dramatically, especially for less particle
12 viscous dissipation (i.e. large e_n) and large friction velocity. Also, the predicted charge-
13 to-mass ratio is widely distributed from -400 to $+60 \mu\text{C kg}^{-1}$, consistent with the
14 previous measurements of charge-to-mass ratio in pure saltation (Bo et al., 2014;
15 Schmidt et al., 1998; Zheng et al., 2003). In addition to affecting sand transport, midair
16 collisions also affect charge exchanges between saltating particles. When considering
17 midair collisions, the charge-to-mass ratio distribution shifts slightly toward zero as the
18 wind velocity increases, as shown in Figs. 7a-7c.

19

20 **4.3. Effects of 3-D E-field on saltation intensity**

21 By substituting the formulations of the 3-D E-field (i.e. $\lambda_i E_i^*$, $i = 1,2,3$) into our
22 model (i.e. Eq. 8), we then evaluate the effects of 3-D E-field on saltation during storms
23 properly. As shown in Fig. 8, compared to the case without E-field, the vertical
24 component of the E-field (i.e. 1-D E-field) inhibits mass flux, in agreement with
25 previous studies (Kok and Renno, 2008; Zheng et al., 2003). However, the mass flux is
26 enhanced by 3-D E-field, causing the simulated value closer to our measured data.
27 Such enhancement of mass flux by 3-D E-field can be explained by the acceleration of
28 saltating particle due to the streamwise and spanwise components (Fig. S5 in the
29 Supplement).



1 Additionally, we also explore how several sensitive parameters such as the density
2 of charged species ρ_h^0 , the coefficient of restitution e_n , and the E-field intensity
3 factors λ_i affect saltation, as shown in Figs. 9a-9b. It can be seen that 3-D E-field
4 enhances the total mass flux by $\sim 10\%$ at the steady stage of the observed dust storm
5 (Fig. 9a) and even up to $\sim 63\%$ in the case of low friction velocity and high E-field
6 intensity factors (Fig. 9b).

7

8 **5. Discussion**

9 **5.1. First-ever measurements of 3-D E-field in the sub-meter layer**

10 To determine the effects of particle tribo-electrification on saltation precisely, 3-
11 D E-field measurements in the saltation layer (i.e. sub-meter above the ground) is
12 required. Although the E-field measurements, such as Bo and Zheng (2013), Esposito
13 et al. (2016), Kamra (1972), Rudge (1913), Williams et al. (2009), and Zhang et al. (2017)
14 in dust storms are numerous, 3-D E-field in the sub-meter layer have not been studied
15 so far. This is because the traditional atmospheric E-field sensors, such as CS110 sensor
16 manufactured by Campbell Scientific, Inc., have dimensions of $15.2 \times 15.2 \times 43.2$ cm (e.g.
17 Esposito et al., 2016; Yair et al., 2016), which is too large compared to the height of
18 saltation layer. Thus, it will lead to significant disturbances of the ambient E-field.
19 Fortunately, the diameter of the VREFM sensor developed by Lanzhou University is
20 only 2 cm and thus could considerably eliminate the E-field disturbances (Zhang et al.,
21 2017; Zheng, 2013). In this study, using the VREFM sensors, we have measured and
22 characterized the 3-D E-field from 0.05 to 0.7 m height during dust storms for the first
23 time, providing valuable data for investigating the particle tribo-electrification in
24 saltation.

25

26 **5.2. An entirely distinct 3-D E-field in dust storms**

27 As many previous studies, the E-field can be simplified to 1-D (i.e. vertical
28 component) in pure saltation (e.g. Kok and Renno, 2008), since in such cases the
29 magnitude of the streamwise and spanwise components is much less than that of



1 vertical component (Zhang et al., 2014). However, during dust storms, the streamwise
2 and spanwise components are one order of magnitude larger than the vertical
3 component, as mentioned previously. E-field is therefore 3-D. In contrast to the vertical
4 component, which is closely related to the total mass loading (Esposito et al., 2016;
5 Williams et al., 2009), the intense streamwise and spanwise components are
6 aerodynamically created due to the nonuniform transport of charged particles in the
7 horizontal plane (Zhang et al., 2014).

8 Our measurements show that the vertical component increases with increasing
9 height in the saltation layer. By contrast, previous studies showed a monotonically
10 decreasing vertical component with increasing height in pure saltation (Kok and Renno,
11 2008; Schmidt et al., 1998). This suggests that the pattern of E-field in dust storms is
12 quite different from that in pure saltation. Because unlike pure saltation, whose E-field
13 is only generated by the charged saltating particles, the highly charged suspended fine
14 dust particles or mineral dust aerosols in dust storms also contribute to the total E-
15 field in the saltation layer.

16

17 **5.3. Particle-particle tribo-electrification resolved model**

18 Although most physical mechanisms, such as asymmetric contact, polarization by
19 external E-fields, statistical variations of material properties and shift of aqueous ions,
20 are responsible for particle electrification, contact or tribo-electrification is the
21 primary mechanism (e.g. Harrison et al., 2016; Lacks and Sankaran, 2011; Zheng, 2013).
22 In previous model, however, the charge-to-mass ratios of the saltating particles are
23 either assumed to be a constant value (e.g. Schmidt et al., 1998; Zhang et al., 2014;
24 Zheng et al., 2003), or are not accounted for in the particle-particle midair collisions
25 (e.g. Kok and Renno, 2008). In this study, by using DEM together with an asymmetric
26 contact electrification model, we explicitly account for the particle-particle tribo-
27 electrification during midair collisions in saltation. The DEM implemented by cell-
28 based algorithms is robust enough to detect and evaluate all particle-particle midair
29 collisional dynamics. Meanwhile, the charge transfer between colliding particles can



1 be determined by Eq. (25). Compared to the previous studies (e.g. Kok and Lacks, 2009),
2 the main innovation of this model is that the comprehensive consideration of the
3 particle collisional dynamics affecting particle charge transfer is involved. In summary,
4 the present model is a particle-particle midair collision resolved model, and the
5 predicted charge-to-mass ratio agrees well with the published measurement data (see
6 Fig. 6c). These findings indicate that midair collisions in saltation are important, both
7 in momentum and charge exchanges.

8

9 **5.4. Implications for evaluating particle tribo-electrification in dust events**

10 It is generally accepted that E-field could considerably affect the lifting and
11 transport of sand particles. As the findings of previous 1-D E-field models (e.g. Kok and
12 Renno, 2008), the E-field has been proven to inhibit sand transport in our model, when
13 considering the vertical component of the E-field alone. In contrast to the 1-D E-field,
14 our model further shows that the real 3-D E-field in dust storms enhances sand
15 transport substantially, consistent with a recent measurement by Esposito et al. (2016).
16 This 3-D E-field model successfully resolves the discrepancy between the 1-D E-field
17 model (e.g. Kok and Renno, 2008) and the recent measurement (i.e. Esposito et al.,
18 2016). Also, the model predicts that the 3-D E-field could enhance the total mass flux
19 by up to 63 % and should therefore not be neglected in future studies.

20 A remaining critical challenge is still to simulate 3-D E-field in dust storms precisely.
21 Because electrical effects in dust storms are very complex, where the atmospheric
22 turbulent flows, particle motion, and particle tribo-electrification are mutually coupled.
23 For example, to model particle tribo-electrification properly, the time steps of DEM are
24 generally from 10^{-7} to 10^{-4} s (Norouzi et al., 2016). However, dust storms have the large
25 spatial extent of up to several hundreds of kilometres and could last more than several
26 tens of hours (Shao, 2008). Such large size and long-term simulations need huge
27 computational costs.

28

29 **6. Conclusions**



1 Severe dust storms occurring in arid and semiarid regions threaten human lives
2 and result in substantial economic damages. Intense E-field up to $\sim 100 \text{ kV m}^{-1}$ does
3 exist in dust storms and could strongly affect particle dynamics. In this study, we
4 performed the first-ever measurements of 3-D E-field in the sub-meter layer from 0.05
5 to 0.7 m above the ground during dust storms by VREFM sensors. Additionally, by
6 introducing the DEM and asymmetric charging mechanism into the saltation model,
7 we numerically study the effects of 3-D E-field on saltation. Overall, our results show
8 that: (1) measured 3-D E-field data nearly collapse on the 3-order polynomial curves
9 when normalized, providing a detailed characterization of the 3-D E-field during dust
10 storms for the first time; (2) the inclusion of 3-D E-field in saltation model can resolve
11 the discrepancy between previous 1-D E-field model (e.g. Kok and Renno, 2008) and
12 measurements (Esposito et al., 2016) in the aspect of whether the E-field inhibits or
13 enhances saltation; (3) midair collisions dramatically affect both momentum and
14 charge exchanges between saltating particles; and (4) the model predicts that 3-D E-
15 field enhances the total mass flux by up to 63 %, suggesting that 3-D E-field should be
16 considered in future models, especially for dust storms.

17 We have also performed discussions about various sensitive parameters such as
18 the density of charged species, the coefficient of restitution, and the E-field intensity
19 factors. These results significantly add new knowledge to the role of particle tribo-
20 electrification in determining the transport and lifting of sand and dust particles.

21

22 **Data availability**

23 The E-field data recorded in our field campaign are provided as a CSV file in the
24 Supplement.

25

26 **Author contribution**

27 H.Z. performed the field observations, numerical simulation, and data analyses as
28 well as wrote the manuscript, which was guided and edited by Y.H.Z. All authors
29 discussed the results and commented on the manuscript.



1

2 **Competing interests**

3 The authors declare that they have no conflict of interest.

4

5 **Acknowledgments**

6 This work was supported by the National Natural Science Foundation of China
7 (grant numbers 11802109 and 11490553), the Young Elite Scientists Sponsorship
8 Program by CAST (grant number 2017QNRC001), and the Fundamental Research
9 Funds for the Central Universities (grant number lzujbky-2018-7).

10

11 **References**

12 Ai, J., Chen, J. F., Rotter, J. M., and Ooi, J. Y.: Assessment of rolling resistance models in
13 discrete element simulations, *Powder Technol.*, 206, 269–282,
14 doi:10.1016/j.powtec.2010.09.030, 2011.

15 Anderson, R. S., and Hallet, B.: Sediment transport by wind: toward a general model,
16 *Geol. Soc. Am. Bull.*, 97, 523-535, doi: 10.1130/0016-
17 7606(1986)97<523:STBWTA>2.0.CO;2, 1986.

18 Anderson, R. S., and Haff, P. K.: Simulation of eolian saltation, *Science*, 241, 820–823,
19 doi:10.1126/science.241.4867.820, 1988.

20 Anderson, R. S., and Haff, P. K.: Wind modification and bed response during saltation
21 of sand in air, *Acta Mech.*, 1, 21–51, doi:10.1007/978-3-7091-6706-9_2, 1991.

22 Bagnold, R.: *The Physics of Blown Sand and Desert Dunes*, Chapman & Hall, London,
23 1941.

24 Bo, T. L., Zhang, H., and Zheng, X. J.: Charge-to-mass ratio of saltating particles in wind-
25 blown sand, *Sci. Rep.*, 4, 5590, doi:10.1038/srep05590, 2014.

26 Bo, T. L., and Zheng, X. J.: A field observational study of electrification with in a dust
27 storm in Minqin, China, *Aeolian Res.*, 8, 39–47, doi:10.1016/j.aeolia.2012.11.001,
28 2013.

29 Brilliantov, N. V., Spahn, F., Hertzsch, J. M., and Poschel, T.: Model for collisions in



- 1 granular gases, *Phys. Rev. E*, 53, 5382, doi:10.1103/PhysRevE.53.5382, 1996.
- 2 Carneiro, M. V., Araújo, N. A., Pähtz, T., and Herrmann, H. J.: Midair collisions enhance
3 saltation, *Phys. Rev. Lett.*, 115, 058001, doi:10.1103/PhysRevLett.111.058001,
4 2013.
- 5 Cheng, N. S.: Simplified settling velocity formula for sediment particle, *J. Hydraul. Eng.*,
6 123, 149–152, doi:10.1061/(ASCE)0733-9429(1997)123:2(149), 1997.
- 7 Dupont, S., Bergametti, G., Marticorena, B., and Simoens, S.: Modeling saltation
8 intermittency, *J. Geophys. Res.-Atmos.*, 118, 7109–7128, doi:10.1002/jgrd.50528,
9 2013.
- 10 Esposito, F., Molinaro, R., Popa, C.I., Molfese, C., Cozzolino, F., Marty, L., Taj-Eddine, K.,
11 Achille, G. D., Franzese, G., and Silvestro, S.: The role of the atmospheric electric
12 field in the dust lifting process, *Geophys. Res. Lett.*, 43, 5501–5508,
13 doi:10.1002/2016GL068463, 2016.
- 14 Haff, P. K., and Anderson, R. S.: Grainscale simulations of loose sedimentary beds: the
15 example of grain-bed impacts in aeolian saltation, *Sedimentology*, 40, 175–198,
16 doi:10.1111/j.1365-3091.1993.tb01760.x, 1993.
- 17 Harrison, R. G., Barth, E., Esposito, F., Merrison, J., Montmessin, F., Aplin, K. L., Borlina,
18 C., Berthelier, J. J., Dprez, G., and Farrell, W. M.: Applications of electrified dust
19 and dust devil electrodynamics to martian atmospheric electricity, *Space Sci. Rev.*,
20 203, 299–345, doi:10.1007/s11214-016-0241-8, 2016.
- 21 Hu, W., Xie, L., and Zheng, X.: Contact charging of silica glass particles in a single
22 collision, *Appl. Phys. Lett.*, 101, 114107, doi:10.1063/1.4752458, 2012.
- 23 Huang, N. E., Shen, Z., Long, S. R., Wu, M. C., Shih, H. H., Zheng, Q., Yen, N. C., Tung, C.
24 C., and Liu, H. H.: The empirical mode decomposition and the Hilbert spectrum
25 for nonlinear and non-stationary time series analysis, *Proc. R. Soc. A-Math. Phys.*
26 *Eng. Sci.*, 454, 903–995, doi:10.1098/rspa.1998.0193, 1998.
- 27 Huang, N. E., and Wu, Z.: A review on Hilbert-Huang transform: Method and its
28 applications to geophysical studies, *Rev. Geophys.*, 46, RG2006,
29 doi:10.1029/2007RG000228, 2008.



- 1 Jackson, T. L., and Farrell, W. M.: Electrostatic fields in dust devils: an analog to Mars,
2 IEEE Trans. Geosci. Remote Sensing, 44, 2942–2949,
3 doi:10.1109/TGRS.2006.875785, 2006.
- 4 Kamra, A. K.: Measurements of the electrical properties of dust storms, J. Geophys.
5 Res., 77, 5856–5869, doi:10.1029/JC077i030p05856, 1972.
- 6 Kawamura, R.: Study on sand movement by wind, Technical Report, Institute of Science
7 and Technology, University of Tokyo, 5, 95–112, 1951.
- 8 Kok, J. F., and Lacks, D. J.: Electrification of granular systems of identical insulators, Phys.
9 Rev. E, 79, 051304, doi:10.1103/PhysRevE.79.051304, 2009.
- 10 Kok, J. F., Parteli, E. J., Michaels, T. I., and Karam, D. B.: The physics of wind-blown sand
11 and dust, Rep. Prog. Phys., 75, 106901, doi:10.1088/0034-4885/75/10/106901,
12 2012.
- 13 Kok, J. F., and Renno, N. O.: Electrostatics in wind-blown sand, Phys. Rev. Lett., 100,
14 014501, doi:10.1103/PhysRevLett.100.014501, 2008.
- 15 Kok, J. F., and Renno, N. O.: A comprehensive numerical model of steady state saltation
16 (COMSALT), J. Geophys. Res.-Atmos., 114, doi:10.1029/2009JD011702, 2009.
- 17 Lacks, D. J., and Sankaran, R. M.: Contact electrification of insulating materials, J. Phys.
18 D-Appl. Phys., 44, 453001, doi:10.1088/0022-3727/44/45/453001, 2011.
- 19 Lettau, K., and Lettau, H. H.: Experimental and micro-meteorological field studies of
20 dune migration, in Lettau, K., and Lettau, H. H., eds., Exploring the World's Driest
21 Climate, Institute for Environmental Studies, University of Wisconsin Madison,
22 110–147, 1978.
- 23 Loth, E.: Lift of a spherical particle subject to vorticity and/or spin, AIAA J., 46, 801–
24 809, doi:10.2514/1.29159, 2008.
- 25 Marticorena, B., and Bergametti, G.: Modeling the atmospheric dust cycle: 1. design
26 of a soil-derived dust emission scheme, J. Geophys. Res.-Atmos., 100, 16415–
27 16430, doi:10.1029/95JD00690, 1995.
- 28 Minier, J. P.: Statistical descriptions of polydisperse turbulent two-phase flows, Phys.
29 Rep., 665, 1–122, doi:10.1016/j.physrep.2016.10.007, 2016.



- 1 Norouzi, H. R., Zarghami, R., Sotudeh-Gharebagh, R., and Mostoufi, N.: Coupled CFD-
2 DEM modeling: formulation, implementation and application to multiphase flows,
3 John Wiley & Sons, Chichester, 2016.
- 4 Owen, P. R.: Saltation of uniform grains in air, *J. Fluid Mech.*, 20, 225–242,
5 doi:10.1017/S0022112064001173, 1964.
- 6 Pähtz, T., Omeradžić, A., Carneiro, M. V., Araújo, N. A., and Herrmann, H. J.: Discrete
7 Element Method simulations of the saturation of aeolian sand transport, *Geophys.*
8 *Res. Lett.*, 42, 2063–2070, doi:10.1002/2014GL062945, 2015.
- 9 Rasmussen, K. R., Kok, J. F., and Merrison, J. P.: Enhancement in wind-driven sand
10 transport by electric fields, *Planet Space Sci.*, 57, 804–808,
11 doi:10.1016/j.pss.2009.03.001, 2009.
- 12 Rice, M. A., Willetts, B. B., and McEwan, I. K.: Observations of collisions of saltating
13 grains with a granular bed from high-speed cine-film, *Sedimentology*, 43, 21–31,
14 doi:10.1111/j.1365-3091.1996.tb01456.x, 1996.
- 15 Rudge, W. A. D.: Atmospheric electrification during South African dust storms, *Nature*,
16 91, 31–32, doi:10.1038/091031a0, 1913.
- 17 Schmidt, D. S., Schmidt, R. A., and Dent, J. D.: Electrostatic force on saltating sand, *J.*
18 *Geophys. Res.-Atmos.*, 103, 8997–9001, doi:10.1029/98JD00278, 1998.
- 19 Shao, Y. P.: *Physics and Modelling of Wind Erosion*, Springer Science & Business Media,
20 Heidelberg, 2008.
- 21 Silbert, L. E., Ertaş, D., Grest, G. S., Halsey, T. C., Levine, D., and Plimpton, S. J.: Granular
22 flow down an inclined plane: Bagnold scaling and rheology, *Phys. Rev. E*, 64,
23 051302, doi:10.1103/PhysRevE.64.051302, 2001.
- 24 Sørensen, M.: On the rate of aeolian transport, *Geomorphology*, 59, 53–62,
25 doi:10.1016/j.geomorph.2003.09.005, 2004.
- 26 Tuley, R., Danby, M., Shrimpton, J., and Palmer, M.: On the optimal numerical time
27 integration for lagrangian dem within implicit flow solvers, *Comput. Chem. Eng.*,
28 34, 886–899, doi:10.1016/j.compchemeng.2009.10.003, 2010.
- 29 White, B. R., and Schulz, J. C.: Magnus effect in saltation, *J. Fluid Mech.*, 81, 497–512,



- 1 doi:10.1017/S0022112077002183, 1977.
- 2 Williams, E., Nathou, N., Hicks, E., Pontikis, C., Russell, B., Miller, M., and Bartholomew,
3 M. J.: The electrification of dust-lofting gust fronts (haboobs) in the sahel, *Atmos.*
4 *Res.*, 91, 292–298, doi:10.1016/j.atmosres.2008.05.017, 2009.
- 5 Wu, Z., Huang, N. E., Wallace, J. M., Smoliak, B. V., and Chen, X.: On the time-varying
6 trend in global-mean surface temperature, *Clim. Dyn.*, 37, 759–773,
7 doi:10.1007/s00382-011-1128-8, 2011.
- 8 Xie, L., Ling, Y., and Zheng, X.: Laboratory measurement of saltating sand particles’
9 angular velocities and simulation of its effect on saltation trajectory, *J. Geophys.*
10 *Res.-Atmos.*, 112, D12116, doi:10.1029/2006JD008254, 2007.
- 11 Yair, Y., Katz, S., Yaniv, R., Ziv, B., and Price, C.: An electrified dust storm over the Negev
12 desert, Israel, *Atmos. Res.*, 181, 63–71, doi:10.1016/j.atmosres.2016.06.011,
13 2016.
- 14 Zhang, H., Bo, T. L., and Zheng, X.: Evaluation of the electrical properties of dust storms
15 by multi-parameter observations and theoretical calculations, *Earth Planet. Sci.*
16 *Let.*, 461, 141–150, doi:10.1016/j.epsl.2017.01.001, 2017.
- 17 Zhang, H., and Zheng, X.: Quantifying the large-scale electrification equilibrium effects
18 in dust storms using field observations at Qingtu Lake Observatory, *Atmos. Chem.*
19 *Phys.*, 18, 17087–17097, doi:10.5194/acp-18-17087-2018, 2018.
- 20 Zhang, H., Zheng, X. J., and Bo, T. L.: Electrification of saltating particles in wind-blown
21 sand: Experiment and theory, *J. Geophys. Res.-Atmos.*, 118, 12,086-12,093.
22 doi:10.1002/532 2013JD020239, 2013.
- 23 Zhang, H., Zheng, X. J., and Bo, T. L.: Electric fields in unsteady wind-blown sand, *Eur.*
24 *Phys. J. E*, 37, 13, doi:10.1140/epje/i2014-14013-6, 2014.
- 25 Zheng, X. J.: Electrification of wind-blown sand: recent advances and key issues, *Eur.*
26 *Phys. J. E*, 36, 138, doi:10.1140/epje/i2013-13138-4, 2013.
- 27 Zheng, X. J., Huang, N., and Zhou, Y. H.: Laboratory measurement of electrification of
28 wind-blown sands and simulation of its effect on sand saltation movement, *J.*
29 *Geophys. Res.-Atmos.*, 108, doi:10.1029/2002JD002572, 2003.
- 30



1 **Table 1.** Description of all variables used in this study.

Symbols	Physical meaning	Units
$a_{0,i}, a_{1,i}, a_{2,i}, a_{3,i}$	fitting coefficients in Eq. 6	1
C_d	drag coefficient	1
C_m	normalized spin lift coefficient in Magnus force formula	1
d_p	particle diameter	m
d_i, d_j	diameters of particle i and j	m
d_m	mean diameter of particle sample in the numerical model	m
D_{imp}, D_{ej}^k	diameter of the impact and ejected particles	m
e_n	coefficient of restitution of particles	1
$E(t)$	a time series of measured E-field	kV m ⁻¹
$\bar{E}(t)$	time-varying mean values of $E(t)$	kV m ⁻¹
$\langle \bar{E}_i(t) \rangle$	height-averaged time-varying mean values of $E(t)$	kV m ⁻¹
$E_i^*(t)$	dimensionless E-field of component i	1
E_1, E_2, E_3	streamwise, spanwise, and vertical components of E-field	kV m ⁻¹
\vec{F}_i^d, \vec{F}_i^m	drag force and Magnus force acting on particle i	N
$\vec{F}_{ij}^d, \vec{F}_{ij}^t$	the normal and tangential collisional forces	N
$g=9.81$	gravitational acceleration	m s ⁻²
G	shear modulus of particles	Pa
G^*	equivalent shear modulus between two contacting particles	Pa
I_i	moment of inertia of particle i	kg m ²
L_x, L_y	streamwise and spanwise width of the computational domain	m
m^*	equivalent particle mass between two contacting particles	kg
$m_{p,i}$	mass of particle i	kg
$\vec{M}_i^{w-p}, \vec{M}_{ij}^c, \vec{M}_{ij}^r$	torque due to the wind, the torque due to the tangential component of the particle collisional forces, and the rolling resistance torque	N·m
\vec{n}_{ij}	unit vector in the direction from the center of particle i point toward the center of particle j	-
N_k	number of ejected particles from the k -th particle bin	1
p_k	mass fraction of the k -th particle bin	1
P_{reb}	rebouncing probability of a saltating particle colliding with the sand bed	1
R^*	equivalent particle radius between two contacting particles	m
Re_p	particle Reynolds number	1
S_i, S_j	contact area of particle i and j	m ²
\vec{u}_r	particle-to-wind relative velocity	m s ⁻¹
u_m	mean streamwise wind speed	m s ⁻¹
u_*	friction velocity	m s ⁻¹
$\vec{u}_{p,i}$	velocity of particle i	m s ⁻¹
$u_{p,i}, w_{p,i}$	streamwise and vertical components of particle velocity	m s ⁻¹
v_{imp}	impact speed of the saltating particle	m s ⁻¹
$\vec{v}_{ij}, \vec{v}_{ij}^n, \vec{v}_{ij}^t$	relative velocity between particle i and j at the contact point, and its normal and tangential components	m s ⁻¹
\vec{x}_i, \vec{x}_j	position vectors of particle i and j	m
$Y=10^8$	Young's modulus of particles	Pa



Table 1. Continued.

Symbols	Physical meaning	Units
Y^*	equivalent Young's modulus between two contacting particles	Pa
z, z^*	height above the ground and dimensionless height	m, 1
z_0	the aerodynamic roughness	m
z_{salt}	saltation height	m
β	damping coefficient of collisional forces	1
$\gamma_s=0.5, \gamma_r=0.1$	coefficients of static and rolling friction	1
$\zeta_{p,i}$	charge-to-mass ratio of particle i	C kg ⁻¹
η_n	residue of EMD	-
θ, φ	rebouncing angles of particles	°
$\kappa \approx 0.41$	von Kármán constant	1
λ_i	E-field intensity factors	kV m ⁻¹
τ_p	particle momentum flux	Pa
$\vec{\omega}_{p,i}$	angular velocity of the particle i	rad s ⁻¹
δ_n, δ_t	normal and tangential overlap between two contacting particles	m
$\mu=1.8 \times 10^{-5}$	dynamic viscosity of the air	Pa·s
$\nu=0.3$	Poisson's ratio of particles	1
ξ_i	Intrinsic mode functions of EMD	-
$\rho_a=1.174$	air density	kg m ⁻³
$\rho_p=2650$	particle mass density	kg m ⁻³
ρ_c	space charge density	C m ⁻³
ρ_h^i, ρ_h^j	density of the electrons trapped in the high energy states on the surface of particle i and j	m ⁻²
σ	surface charge density	C m ⁻²
σ_p	geometric standard deviation of particle sample in the numerical model	1
Δq_{ij}	net increment of the charge of particle i after colliding with particle j	C
Δz	vertical grid size	m

1

2



1 **Table 2.** Fitting coefficients of the 3-order polynomial curves in Figs. 5a-5c.

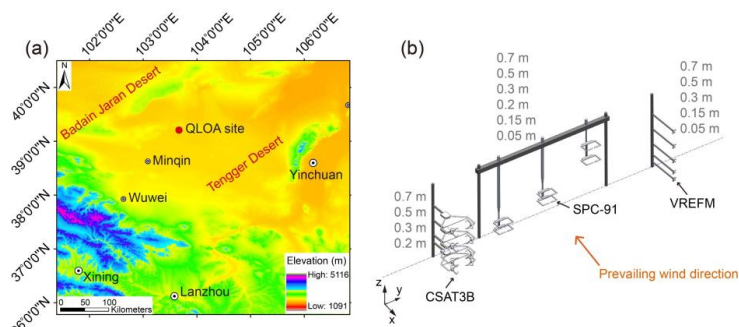
Components	$a_{0,i}$	$a_{1,i}$	$a_{2,i}$	$a_{3,i}$	R^2
$i = 1$	-0.59	2.30	-2.66	0.72	0.52
$i = 2$	-0.23	0.71	-1.18	0.16	0.61
$i = 3$	0.13	-0.20	1.96	-0.83	0.60

2

3



1



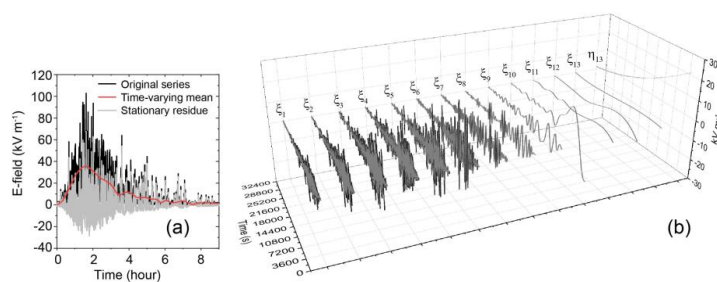
2

3 **Figure 1.** Map of the QLOA site and the layout of all instruments. (a) The QLOA site is
4 located between the Badain Jaran Desert and the Tengger Desert, approximately 90
5 km northeast of Minqin, Gansu, China. (b) Four CSAT3B sensors were mounted at 0.2-
6 0.7 m height, respectively; six SPC-91 sensors were mounted at 0.05-0.7 m height,
7 respectively; total fifteen VREFM sensors were mounted to measure the 3-D E-field at
8 0.05-0.7 m height, respectively (that is, at each measurement point, three VREFM
9 sensors are mutually perpendicular). The CSAT3B, SPC-91, and VREFM sensors were
10 distributed along a straight line parallel to the y axis, and the prevailing wind
11 direction in the QLOA site is parallel to the x axis.

12



1



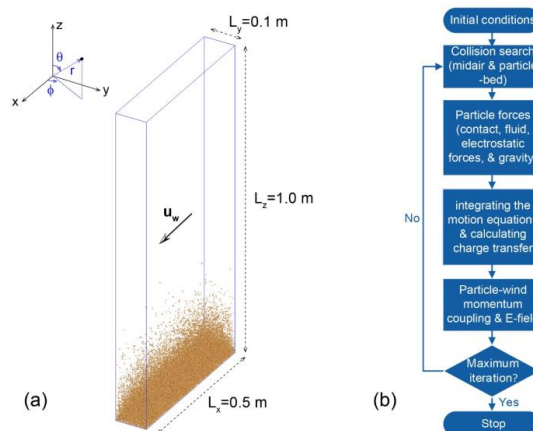
2

3 **Figure 2.** The resulting EMD components from a measured E-field time series. (a) The
4 original measured time series, the time-varying mean (which is defined as the sum of
5 the last four IMFs and the overall trend), and the stationary residue (which is the
6 difference between the original time series and the time-varying mean). (b) Time
7 series of the total 13 IMFs, ξ_1 - ξ_{13} , and the residue (overall trend), η_{13} .

8



1



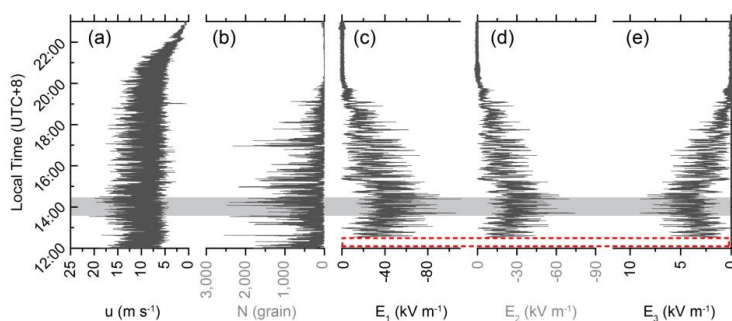
2

3 **Figure 3.** A schematic illustration of the DEM simulation of saltation and the numerical
4 algorithm of the saltation model. (a) A 3-D view of the simulated wind-blown sand at
5 a steady state, where the wind shear velocity $u_* = 0.5 \text{ m s}^{-1}$, average sand diameter
6 $d_m = 228 \text{ }\mu\text{m}$, and geometric standard deviation $\sigma_p = \exp(0.3)$. Both the Cartesian and
7 spherical coordinates are shown in the insert. (b) This flowchart shows the scheme for
8 simulating the saltation according to the following steps implementing the DEM with
9 particle electrification: initial conditions, collision search, particle forces, integrating
10 motion equations and calculating charge transfer, particle-wind momentum coupling
11 and evaluating E-field, and finally repeating these execute steps until reaching the
12 maximum iteration steps.

13



1



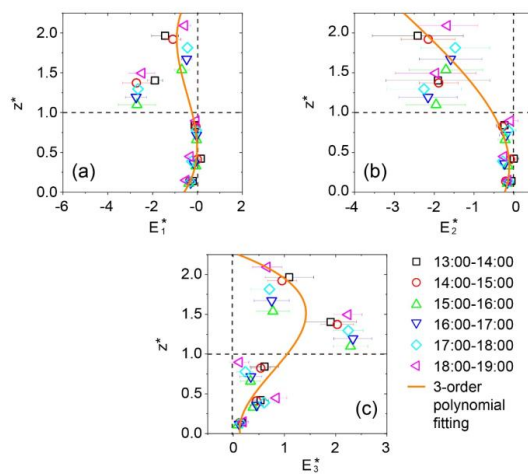
2

3 **Figure 4.** Measured results during a dust storm occurring on May 6, 2014, at QLOA site.
4 (a)-(e): the measured time series of the streamwise wind speed, u at 0.7 m; number
5 of saltating particle N at 0.15 m; streamwise E-field E_1 , spanwise E-field E_2 , and
6 vertical E-field E_3 at 0.7 m. Unfortunately, owing to the interruption of power supply,
7 the 3-D E-field data have not been recorded before $\sim 12:30$, as represented by a dashed
8 box in subgraphs 4c-4e. The shaded area denotes the relatively stationary period of
9 the observed dust storm.

10



1



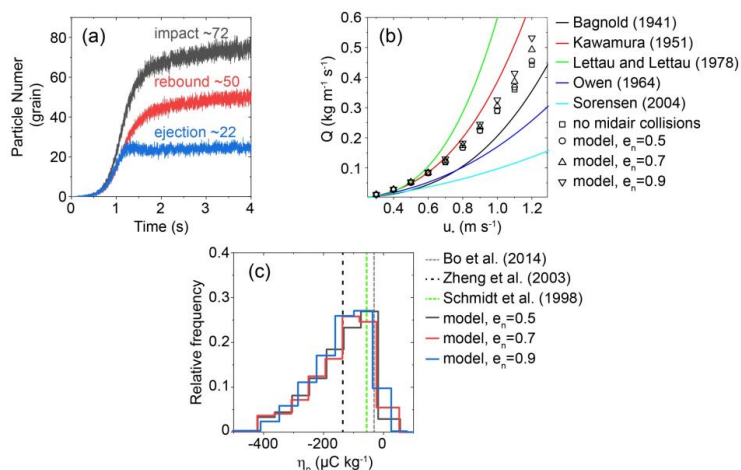
2

3 **Figure 5.** Vertical profiles of the normalized 3-D E-field. Subgraphs (a)-(c), in turn,
4 correspond to the vertical profiles of E_1^* , E_2^* , and E_3^* in the different stages of the
5 observed dust storm. Symbols denote the mean values of the normalized E-field data,
6 error bars are standard deviations, and lines denote 3-order polynomial fitting of the
7 normalized E-field data (with R^2 of 0.52, 0.61, and 0.64, respectively).

8



1



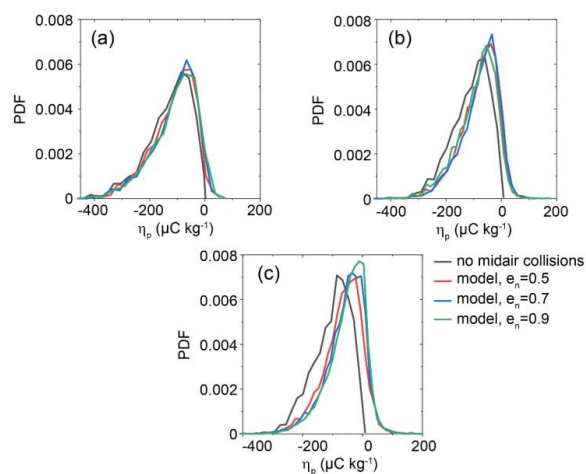
2

3 **Figure 6.** Verification of the steady-state numerical model in the case of pure saltation.
 4 That is, only vertical E-field needs to be considered, which is produced by the charged
 5 saltating particles. (a) Number of the impacting, rebounding, and ejected particles
 6 within each time period of 10^{-4} s, where $u_* = 0.5 \text{ m s}^{-1}$, $d_m = 228 \text{ }\mu\text{m}$, and $\sigma_p = \exp(0.3)$.
 7 (b) Comparison of the simulated total mass flux with the most commonly-used
 8 semiempirical saltation mass flux equations (Bagnold, 1941; Kawamura, 1951; Lettau
 9 and Lettau, 1978; Owen, 1964; Sørensen, 2004), where $d_m = 228 \text{ }\mu\text{m}$, and $\sigma_p = \exp$
 10 (0.3) . (c) Comparison of the simulated charge-to-mass ratio distribution in the range
 11 of 0.07-0.09 m height with the measured mean charge-to-mass ratio, in the range of
 12 0.06-0.1 m height (Zheng et al., 2003), at 0.05 m height (Schmidt et al., 1998) and 0.08
 13 m height (Bo et al., 2014). Here, $\rho_h^0 = 6 \times 10^{15} \text{ m}^{-2}$ is determined by calibrating the model
 14 with measurements; $u_* = 0.35 \text{ m s}^{-1}$, $d_m = 203 \text{ }\mu\text{m}$, and $\sigma_p = \exp(0.33)$ are estimated
 15 from (Zheng et al., 2003).

16



1



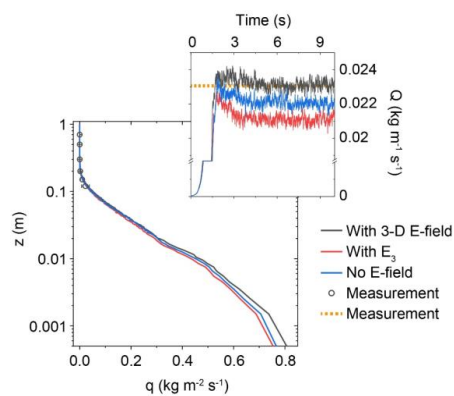
2

3 **Figure 7.** Effects of midair collisions on the probability density function (PDF) of charge-
4 to-mass ratio of saltating particles for various wind velocities (a) $u_* = 0.5 \text{ m s}^{-1}$, (b)
5 $u_* = 0.7 \text{ m s}^{-1}$, and (c) $u_* = 0.9 \text{ m s}^{-1}$, where $d_m = 203 \text{ }\mu\text{m}$, $\sigma_p = \exp(0.33)$, and $\rho_h^0 = 6 \times 10^{15}$
6 m^{-2} .

7



1



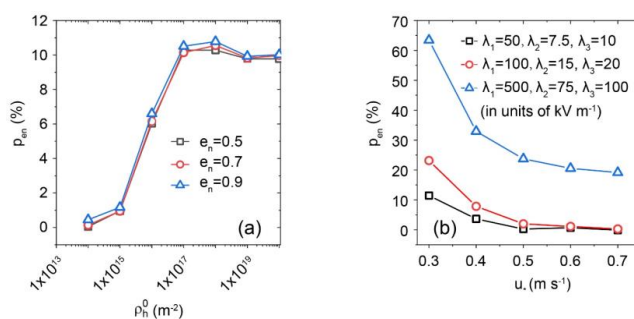
2

3 **Figure 8.** Comparison of the simulated mass flux profile and total mass flux with our
4 measurements, where $u_* = 0.37 \text{ m s}^{-1}$, $d_m = 200 \text{ }\mu\text{m}$, $\sigma_p = \exp(0.42)$, $\rho_h^0 = 6 \times 10^{15} \text{ m}^{-2}$,
5 and $e_n = 0.7$ are reliably estimated from our measurements.

6



1



2

3 **Figure 9.** Effects of some sensitive parameters. (a) Percent increase in total mass flux,
 4 P_{en} , as a function of ρ_h^0 ranging from 10^{14} to $10^{20} m^{-2}$ (e.g. Kok and Lacks, 2009) for
 5 various e_n at the steady stage of the observed dust storm, as represented by the
 6 shaded area in Figs. 4a-4e. (b) P_{en} as a function of u_* for various E-field intensity
 7 factors, where the case that $\lambda_1=100$, $\lambda_2=15$, and $\lambda_3=20$ $kV m^{-1}$ corresponds to the
 8 steady stage of the observed dust storm. In these cases, $\rho_h^0=1 \times 10^{17} m^{-2}$, $e_n=0.7$.